First Results of Absorbing Aerosol Index From the Absorbing Aerosol Sensor Onboard Gaofen-5B

Zhuo Zhang ⓘ, Jian Xu ⓘ, *Senior Member, IEEE*, Yongmei Wang ⓘ, Entao Shi, Pengfei Zhang, Shun Yao, Jun Zhu, Lanlan Rao ⓘ, Houmao Wang, and Jinghua Mao ⓘ

Abstract—The Absorbing Aerosol Index (AAI) determines the presence and approximate amount of absorbing aerosol particles. The Absorbing Aerosol Sensor (AAS) equipped on the Gaofen-5B satellite was successfully launched and deployed in orbit on September 7, 2021. Following a period of initial on-orbit testing, reliable AAI observational results were collected. The nadir of the AAS had a design spatial resolution of 4 km × 4 km and a current spatial resolution of 2 km × 4 km, which presented significant benefits in the spatial resolution and clear distribution characteristics of pollutants. The results of AAS were validated by comparing with the observed data of Global Ozone Monitoring Experiment-2 (GOME-2) in the Sahara Desert and surrounding areas. In 2022 and 2023, we utilized AAS observations to study the typical pollution processes. These included the spring pollution distribution around the Bohai Sea, the observation and tracking of long-term dust pollution in China in March and April 2023, the distribution of spring pollution in the Indochina Peninsula in April 2023, and the distribution of wildfires in Canada on June 22, 2023. The results were validated and analyzed using data from Tropospheric Monitoring Instrument (TROPOMI), GOME-2, AErosol RObotic NETwork (AERONET) and Moderate-resolution Imaging Spectroradiometer (MODIS). The results of the observation and evaluation revealed that the AAS AAI can provide reliable information for precise observation of air pollutants at a high resolution.

Index Terms—Aerosols, atmospheric measurements, information retrieval, remote sensing, satellite applications.

Zhuo Zhang, Entao Shi, Houmao Wang, and Jinghua Mao are with the Laboratory of Space Environment Exploration, National Space Science Center, Chinese Academy of Sciences, Beijing 100190, China, also with the Beijing Key Laboratory of Space Environment Exploration, Beijing 100190, China, and also with the Key Laboratory of Environmental Space Situation Awareness Technology, Beijing 100190, China (e-mail: zhangzhuo@nssc.ac.cn; set@nssc.ac.cn; hmwang@nssc.ac.cn; maojinghua@nssc.ac.cn).

Jian Xu and Lanlan Rao are with the Key Laboratory of Microwave Remote Sensing, National Space Science Center, Chinese Academy of Sciences, Beijing 100190, China (e-mail: xujian@nssc.ac.cn; raolanlan@nssc.ac.cn).

Yongmei Wang is with the Laboratory of Space Environment Exploration, National Space Science Center, Chinese Academy of Sciences, Beijing 100190, China, also with the Beijing Key Laboratory of Space Environment Exploration, Beijing 100190, China, also with the Key Laboratory of Environmental Space Situation Awareness Technology, Beijing 100190, China, and also with the School of Astronomy and Space Science, University of Chinese Academy of Sciences, Beijing 100049, China (e-mail: wym@nssc.ac.cn).

Pengfei Zhang is with the Shanghai Institute of Satellite Engineering, Shanghai 201109, China (e-mail: chungpf2000@163.com).

Shun Yao and Jun Zhu are with the DFH Satellite Company Ltd., Beijing 100081, China (e-mail: sugeryao@163.com; 12393692@qq.com).

Digital Object Identifier 10.1109/JSTARS.2024.3439014

I. INTRODUCTION

AEROSOL particulate matter is one of the main pollution components in the atmosphere. Small aerosol particles, such as PM2.5, can penetrate deep into the respiratory system and pose short- and long-term health risks to humans [1], [2]. The larger particles of pollutants will affect visibility and seriously interfere with human activities. It is important to evaluate and control the environmental pollution caused by aerosols [3]. Aerosol particles affect the radiation field in the atmosphere by scattering and absorbing light. In the short term, changes in this radiation field can affect the weather, and long-term changes can have an impact on the climate [4], [5]. Global observation of aerosol can better assess the impact of aerosols on the atmospheric radiation force, thus contributing to the study of climate change. Spaceborne detectors can achieve global observation of aerosols with wide coverage. High spatial resolution satellite aerosol observation products can provide reliable data for the monitoring of aerosol pollutants and the assessment of aerosol impacts on climate [6].

The Absorbing Aerosol Index (AAI) can effectively monitor atmospheric pollutants, such as dust, industrial emissions, biomass combustion, volcanic smoke, and certain types of carbonaceous aerosols that exhibit absorbing optical characteristics [7]. The superiority of the AAI is that it is less affected by surface albedo and is available in the presence of thin clouds. High-resolution AAI data are valuable for observing and preventing air pollution. The index was first introduced to correct errors in total ozone retrieval caused by the presence of aerosols [8]. The total ozone mapping spectrometer (TOMS) of the Nimbus-7 satellite was the first to provide AAI products [9]. The Global Ozone Monitoring Experiment (GOME)/GOME-2 [10], Scanning Imaging Absorption spectroMeter for Atmospheric CHartographY (SCIAMACHY) [11], Ozone Monitoring Instrument (OMI) [12], Ozone Mapping and Profiler Suite (OMPS) [13], and Tropospheric Monitoring Instrument (TROPOMI) [14] have successively provided effective AAI results. This polar-orbiting satellite-based passive ultraviolet visible light atmospheric component detectors offer daily global coverage of AAI products. The main errors for these products include measurement and calibration errors [7], [15], [16], forward model errors [17], errors caused by ozone for certain wavelengths and clouds, errors introduced by surface properties, etc. In addition, the AAI values obtained by different types of aerosols with the same concentration are also different [18].

In China, the Total Ozone Unit on the FengYun-3 satellite was the first to provide AAI data [19], [20], [21], [22]. These data have been utilized in several observational and analytical studies [23], [24]. The Gases Monitoring Instrument (EMI) was launched aboard the Chinese GaoFen-5A satellite in 2018 and has provided AAI products [25]. In addition, the Absorbing Aerosol Sensor (AAS) was launched aboard the GaoFen-5B satellite on September 7, 2021, and the Ozone Monitor Suite-Nadir (OMS-N) was launched aboard the FengYun-3F satellite on August 3, 2023 [26]. The AAS is an imaging spectrometer with a 114° wide swath and a continuous spectrum in the 340–550 nm. With a design spatial resolution of 4 km × 4 km at the nadir, it attains a relatively high spatial resolution within instruments of similar features [27], [28]. Its current practical nadir resolution is 2 km × 4 km. Following a period of on-orbit testing, the device successfully obtained observations of the AAI [29].

As AAS can provide a relatively high spatial resolution of its kind, the analysis of pollution processes using its data can provide a better understanding of atmospheric environmental changes. This study represented the first attempt to track and analyze atmospheric pollution using AAI data from the AAS. We selected several notable air pollution events that occurred between 2022 and 2023, including a springtime air pollution in the Bohai Sea region in March 2022, severe dust pollution across China in March and April 2023, spring pollution in the Indochina Peninsula in April 2023, and wildfires in Canada on June 22 and 2023. Additionally, we utilized AAI data from TROPOMI and GOME-2 to corroborate and validate the findings obtained from AAS using MODIS and ground-based AERONET data to further analyze and verify the observations of pollutants.

II. METHOD AND DATA

A. AAS

At 11:01 on September 7, 2021, China successfully launched a hyperspectral observation satellite (Gaofen-5B). Gaofen-5B officially entered service on April 4, 2023, after two years of in-orbit testing. In contrast to optical imaging satellites, which can only see information such as the shape and size of objects, hyperspectral satellites have spectral imaging technology. Gaofen-5B satellite carries seven payloads, including Advanced Hyperspectral Imager (AHSI), Visual and Infrared Multispectral Imager (VIMI), Directional Polarimetric Camera (DPC), AAS, greenhouse gases monitoring instrument (GMI), Environmental Monitoring Instrument (EMI) and Particulate Observing Scanning Polarimeter (POSP). Covering the spectrum from ultraviolet to long-wave infrared, it integrates imaging technology and hyperspectral detection technology to realize comprehensive observation of spatial information, spectral information, and radiation information. It is another full-spectrum hyperspectral satellite to realize the comprehensive observation of the atmosphere and land after the Gaofen-5 satellite.

The AAS is on a morning a sun-synchronous satellite. The time of the orbit is 11:08 and the orbit height is 705 km. The AAS is a wide field-of-view (FOV) push-broom spectrograph with a 114-degree FOV ensuring it achieves daily global coverage. It

TABLE I
GF-5B/AAS INSTRUMENT PARAMETERS

Parameter	Characteristics
Spectral range (nm)	340–550
Spectral resolution (nm)	< 2.0 nm
FOV	± 57°
Spatial resolution	4×4 km (at nadir)
Calibration accuracy	2%
SNR	>1000 (10.89 μW/cm^2· sr· nm)

can acquire a continuous spectrum from 340 to 500 nm and the spectral resolution is within 2.0 nm. It has a high signal-noise ratio which is higher than 1000. Its primary mission is for monitoring tracking aerosol in the atmosphere. The primary optical properties are listed in Table I [29].

The design nadir spatial resolution of 4 km × 4 km is binned from two 2 km× 4 km nadir pixels. During in-orbit operation, we found it could get effective result even though the nearby two pixels had not been binned. As a result, we increased the nadir spatial resolution to 2 km× 4 km.

B. Retrieval Method

The top-of-atmosphere reflectance ratios of the two channels with minimal ozone absorption in the ultraviolet spectrum are quantified in a real atmosphere. The disparity between this ratio and the simulated ratio of the Rayleigh atmosphere is referred to as the residue [8]. Based on the optical properties of various types of aerosols, absorbing aerosols result in a positive residue known as AAI. In contrast, clouds and scattering aerosols generate a slightly negative or zero residue [7]. The previously mentioned residual γ is defined as follows [30]:

$$\gamma = -100 \cdot \left(\log_{10} \left(\frac{I_\lambda}{I_{\lambda_0}} \right)^{\text{meas}} - \log_{10} \left(\frac{I_\lambda}{I_{\lambda_0}} \right)^{\text{Ray}} \right) \quad (1)$$

where λ and λ_0 are the channels used in the retrieval. For AAS, the central wavelengths of the two channels were 354 nm and 388 nm, respectively, because the bands were less affected by ozone than those at 340 nm and 380 nm. I represents the reflectance at the top of the atmosphere and $^{\text{meas}}$ is the measured value in the real atmosphere. $^{\text{Ray}}$ is for the simulated value in pure Rayleigh atmosphere.

AAI is a dimensionless, semiquantitative measure that reflects the presence or absence of absorbing aerosol pollutants, as well as the approximate level of pollution. In this study, the SCIATRAN radiative transmission model [31] was utilized to perform the inversion process. The specific steps of the retrieval are as follows.

1) We retrieved the preliminary global AAI distribution using the method mentioned earlier.
2) We used a wavelength of 388 nm to determine the cloud fraction, assuming a Lambertian surface, which is not entirely accurate and introduces some traces of clouds above complex terrains, such as the Hengduan Mountains.

3) We set the average AAIs of cloudless and uncontaminated pixels in the Pacific Ocean as background values. These cloudless and uncontaminated pixels were obtained by modeling and observing reflectance [25].

4) Thick cloud (cloud fraction> 0.5) pixels were removed, and the background was subtracted to obtain the final AAI result.

Because of the time-consuming nature of acquiring the background, the current background resolution along the track was 1°, whereas the resolution along the cross-orbit direction was the same as the pixel spatial resolution. The along-track resolution would be optimized in the future. The L1 data can be accessed at https://data.cresda.cn/#/home.

Preliminary validation was conducted in a previous study [29]. In this study, we used the AAI product to observe several pollution processes.

C. Other Data

1) AAI From GOME-2 and TROPOMI: GOME-2 is a satellite-based ozone monitoring instrument installed on the METOP satellite that employs a UV-visible medium-resolution sky and earth scanning spectrometer with a spectral range of 240–790 nm. The AAI product generated by GOME-2 had a spatial resolution of 1°. METOP is a morning satellite, and its transit time is close to that of the AAS, making it a useful tool for validating the AAS results. GOME-2 AAI showed good consistency compared with SCIAMACHY AAI in an intercomparison approach. A clear linear relationship is between the GOME-2 AAI and the SCIAMACHY AAI. Also, the slope of the linear fit is close to one. The bias-corrected uncertainty in the GOME-2 AAI was found to be ~0.5 index point [32].

TROPOMI is a four-channel UV-VIS-NIR-SWIR imaging spectrometer with a 114° field of view and a nadir spatial resolution of 3.5 km × 5.5 km in the afternoon satellite. The data obtained from TROPOMI are accessible on the website: https://s5phub.copernicus.eu. The comparison of TROPOMI and OMI observation results in a typical pollution event is consistent [33]. In addition to those sources of error mentioned in Section I, the BRDF of clouds also has a strong impact on the AAI [34].

This study utilized the 354 nm/388 nm wavelength pair of AAI products, which can be available for both the GOME-2 and TROPOMI instruments.

2) Aerosol Optical Depth From AERONET: The AErosol RObotic NETwork (AERONET) is a ground-based remote sensing aerosol network, providing globally distributed observations of aerosol optical depth (AOD) at various wavelengths. The version 3 observation data involves three data quality levels: Level 1.0 (unscreened), Level 1.5 (cloud-screened and quality-controlled), and Level 2.0 (quality-assured). Level 2.0 data are rare for the target area and time duration. Therefore, in this study, we employed Level 1.5 daily averaged SDA 500 nm AOD and 500 nm Fine Mode Fraction data. The data website is https://aeronet.gsfc.nasa.gov/new_web/index.html. Fig. 1 depicts the distribution of four AERONET ground-based sites we selected from four countries in the Indochina Peninsula for the case in Section IV-D.
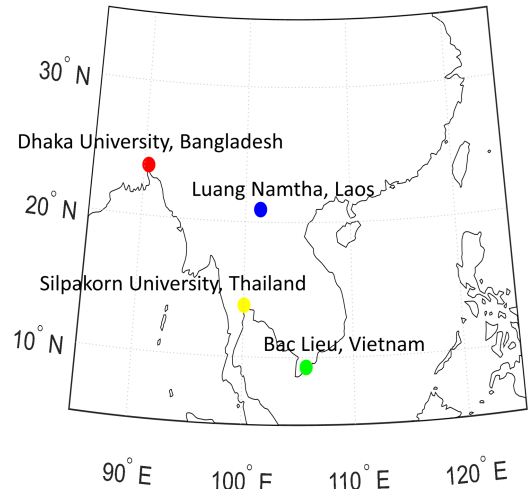

Fig. 1. Four selected AERONET sites in the target area in Section IV-D, including sites in Bangladesh (red), Laos (blue), Thailand (yellow), and Vietnam (green).

TABLE II
GF-5B/AAS AAI ERROR ANALYSIS

Source	Uncertainty	Error
Calibration error	2%	0.28−0.27
Equivalent surface albedo	0.001	0.009
Surface pressure (kPa)	0.001	0.01

3) True Color Corrected Reflectance From Terra/MODIS: To assess the pollution conditions, we consulted the color-corrected reflectance v6.1 standard data from Terra/MODIS which shows smoke more clearly than the standard surface reflectance product [35], [36]. This data can be accessed through the website https://worldview.earthdata.nasa.gov/.

III. ERROR ANALYSIS AND VALIDATION

To make an accurate retrieval, the information of the relative location between the aerosol layer and cloud layer is necessary [7]. In order to eliminate the interference caused by incomplete cloud information in error analysis, error analysis is carried out by using cloud-free (cloud fraction = 0) pixel data of the Pacific Ocean. The effects of calibration error, equivalent surface albedo, and surface pressure on AAI inversion results are analyzed by only changing the parameter being examined in AAI retrieval. The calibration error of the detector is 2% getting from calibration experiments, which will cause a deviation of 0.28 to −0.27 to the final observation result. The accuracy of equivalent surface reflectance calculated in inversion is 0.001, and the error is 0.009. The accuracy of the surface elevation is 0.001 kPa, resulting in an error of 0.01. The error analysis result is shown in Table II.

Because there are dust particles in the Sahara Desert all the year round, AAI observation cases with a large numerical range can be provided. Like AAS, GOME-2 is also aboard a morning satellite. A few days of AAS observation data were compared with GOME-2 observation data to evaluate the accuracy of AAS observation results. We used data from March 29 and 31 and April 3, 4, 5 and 7, 2024. The latitude and longitude
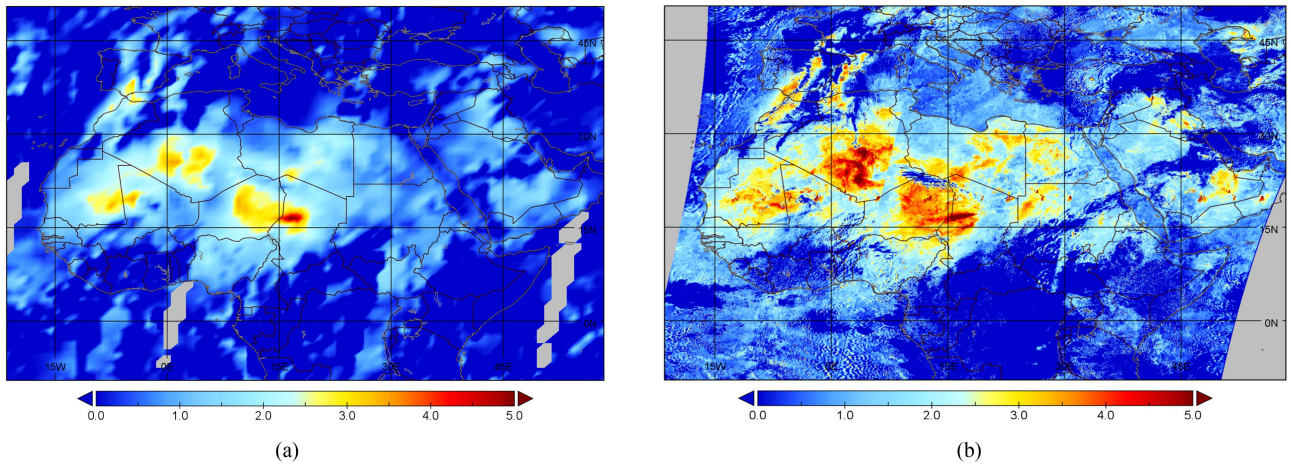
Fig. 2.   Dust in the Sahara on April 7, 2024. (a) AAI from GOME-2. (b) AAI from AAS.
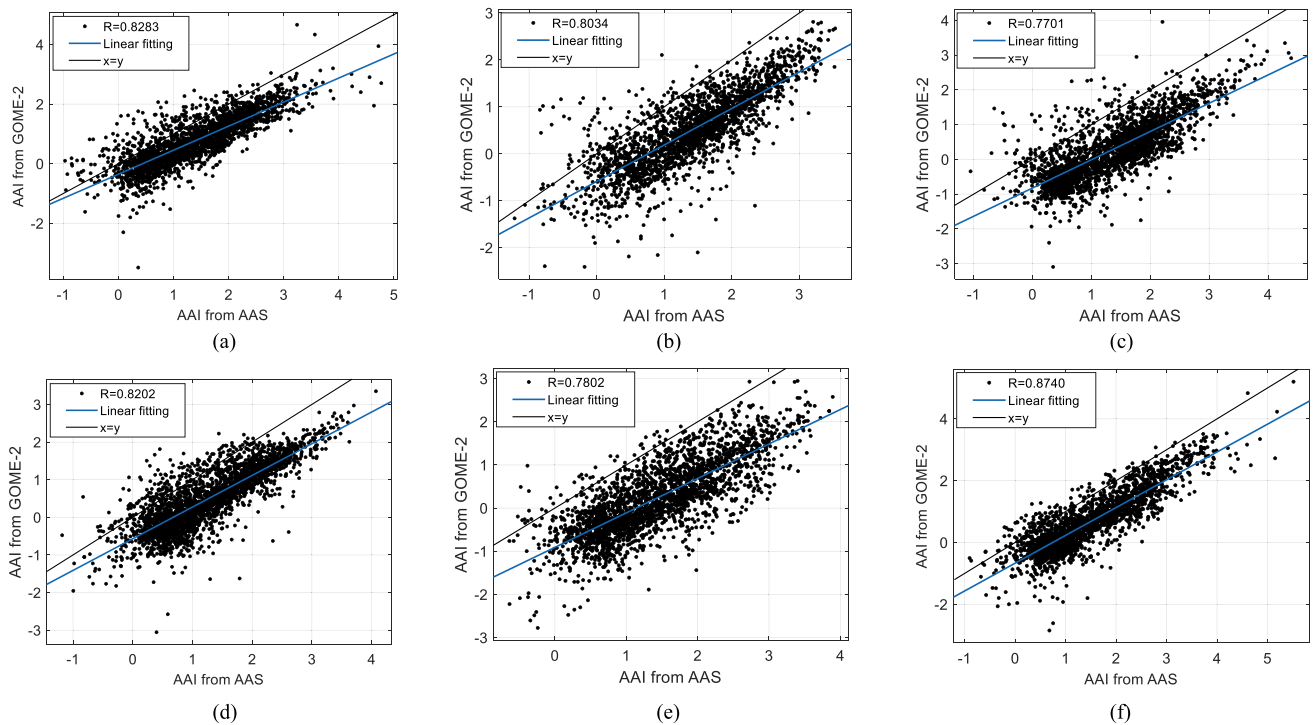

Fig. 3.   Correlation analysis of AAS and GOME-2 observation data for the Sahara region. (a) March 29, 2024. (b) March 31, 2024. (c) April 3, 2024. (d) April 4, 2024. (e) April 5, 2024. (f) April 7, 2024.

of the target region is 23W–60E, 10S–51N. Take the April 7 data as an example. Because of the limited spatial coverage of both MetOp-B/GOME-2 and MetOp-C/GOME-2, we merged the data of the two detectors to obtain the AAI distribution map of GOME-2, as shown in Fig. 2(a). Fig. 2(b) depicts AAI from AAS in the same area. The retrieval wavelength pair used by GOME-2 is 340/380 nm. To avoid the error introduced by ozone in the retrieval, AAS uses 354/388 nm. The AAI obtained by these two wavelength selection methods have a small difference in numerical value, so we mainly investigate the correlation between the two instruments' results. The AAS data were projected onto a $1° \times 1°$ grid of GOME-2 and then averaged. The results are shown in Fig. 3.

As can be seen from the analysis results in Fig. 3(a)–(f), despite a loss of detailed features in the AAS observations after averaging, the correlation coefficients between GOME-2 and AAS results in the 6 days were all about 0.8, and the mean value was 0.8127. This indicates that the retrieval results of AAS are reliable and can be used for pollutant observation.

To assess the accuracy of the AAS observation data during the pollution period in China and the Indochina Peninsula in April 2023, we obtained GOME-2 observation data or comparative analysis and verification. The data from April 11, with the presence of large-scale pollution, were selected for this study. We still merged the data of MetOp-B/GOME-2 and MetOp-C/GOME-2 to obtain the global AAI distribution map of GOME-2 in Fig. 4.
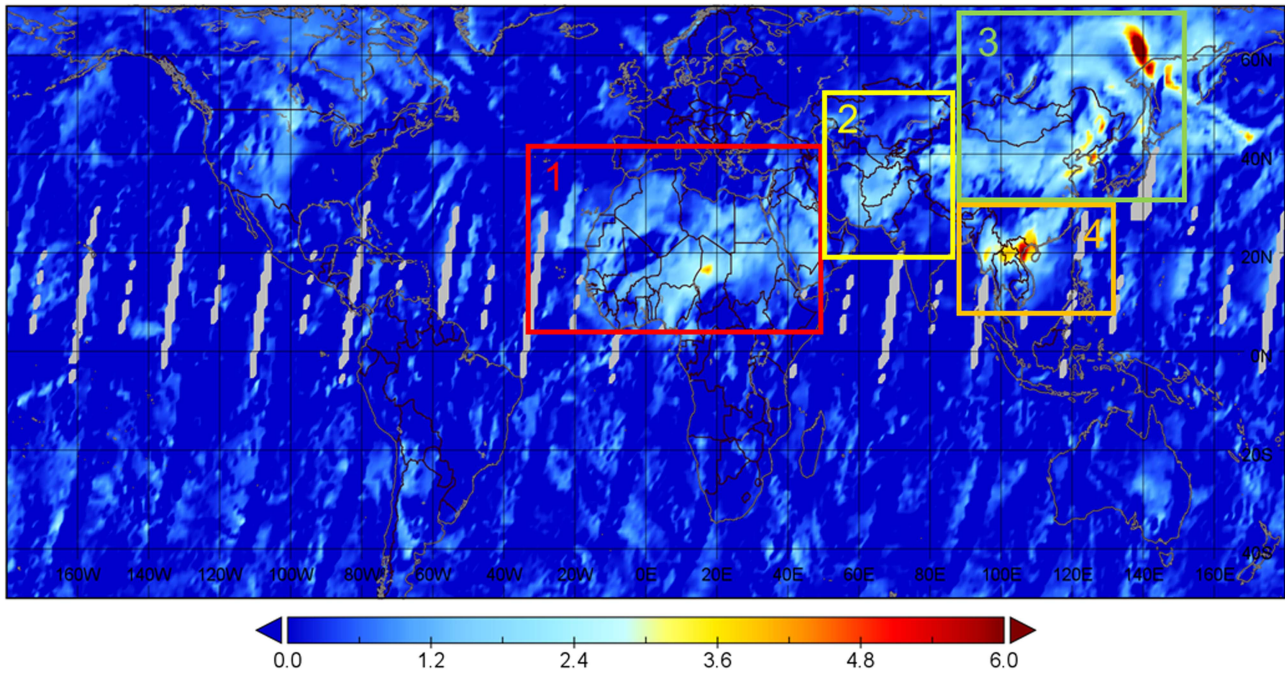
Fig. 4. Merged global AAI distribution from MetOp-B/GOME-2 and MetOp-C/GOME-2 on April 11, 2023. The four square boxes delineate the divisions of the four pollution districts.
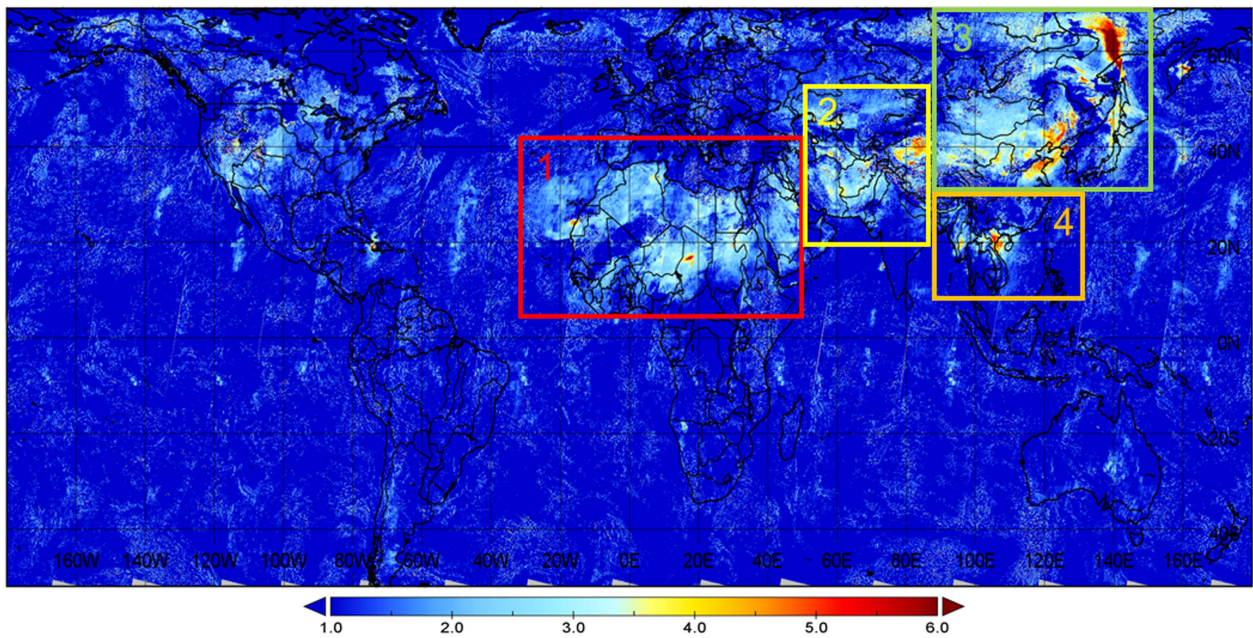

Fig. 5. Global AAI distribution from AAS on April 11, 2023. The four rectangular boxes denote divisions of the four pollution districts.

Fig. 5 presents global AAI observations from the AAS on April 11. We divided the data into four typical pollution districts, using rectangular boxes in the two figures.

The AAS data were projected onto a $1° \times 1°$ grid of GOME-2 and then averaged. Correlations between the average AAS data of the four regions and the observation results of GOME-2 were calculated. The results are shown in Fig. 6. Despite a loss of detailed features in the AAS observations after averaging, the results in Fig. 6 indicate high correlations with GOME-2.

IV. APPLICATION OF AAI FROM AAS IN SEVERAL POLLUTION EVENTS

A. Air Pollution Around Bohai Sea in March 2022

To assess the severe pollution weather that occurred in the Bohai Sea on March 4, 2022, the AAI data obtained from the AAS was compared with the AAI data from TROPOMI (Fig. 7). The overall appearance and distribution of pollutants, as demonstrated by both sources, were highly consistent. Because
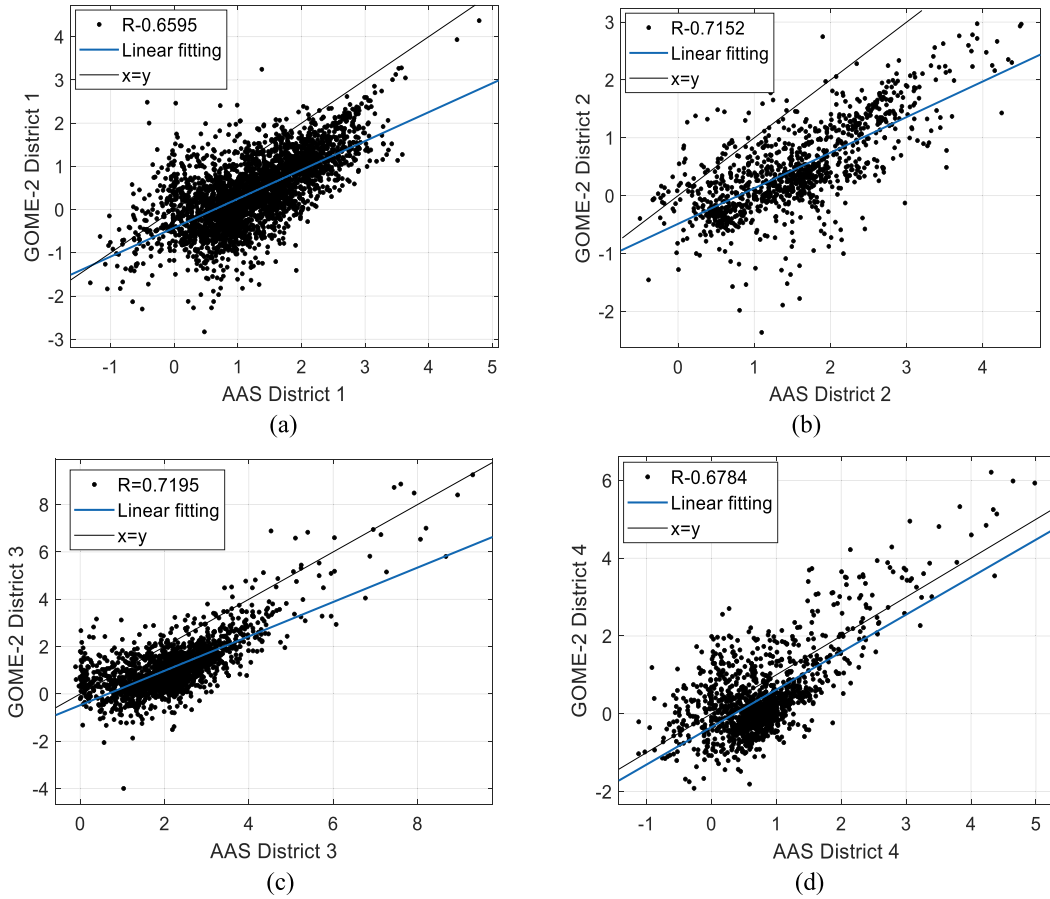
Fig. 6. Correlation analysis of AAS and GOME-2 observation data for the four regions in Figs. 10 and 11. (a) District 1. (b) District 2. (c) District 3. (d) District 4.
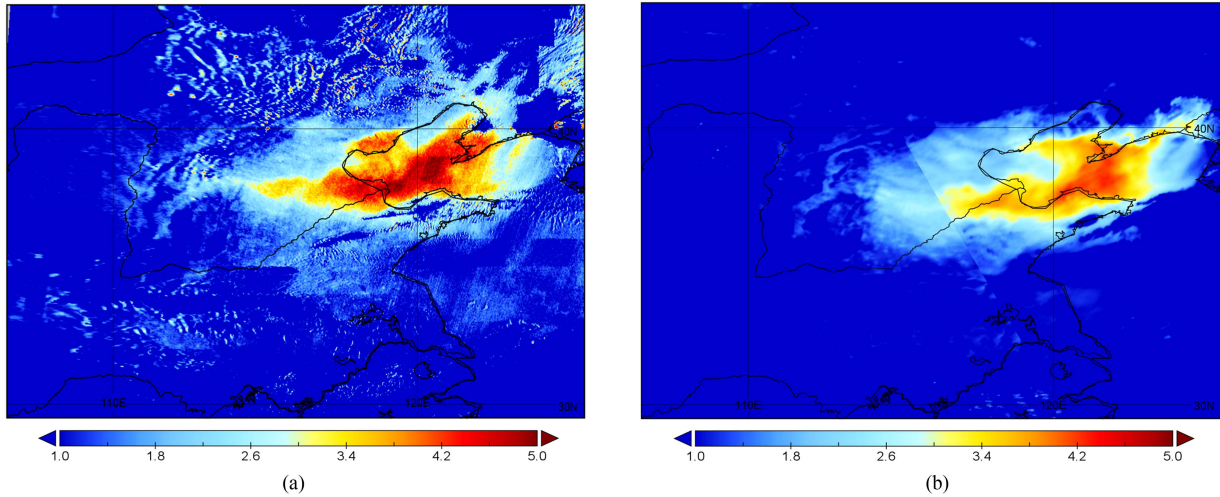
Fig. 7. Air pollution around the Bohai Sea on March 4, 2022. (a) AAI from AAS. (b) AAI from TROPOMI.

Gaofen-5B operated as a morning satellite while TROPOMI was carried on an afternoon satellite, the specific characteristics of the regional distribution of pollutants, as observed by the two sources, exhibited slight variations. Additionally, from a spatial resolution perspective, the AAS was comparable to that of TROPOMI.

B. Dust Pollution Process in North China in March 2023

Since March 2023, the northern region of China has experienced several severe dust pollution events. On March 22, Beijing and its surrounding regions experienced extremely high pollution. To track and analyze the pollution process, the inversion results of the AAI system developed by the AAS were utilized.

Fig. 8. AAI from the AAS observed the dust pollution process in China in March 2023. (a)–(d) Are for March 19–22, respectively.
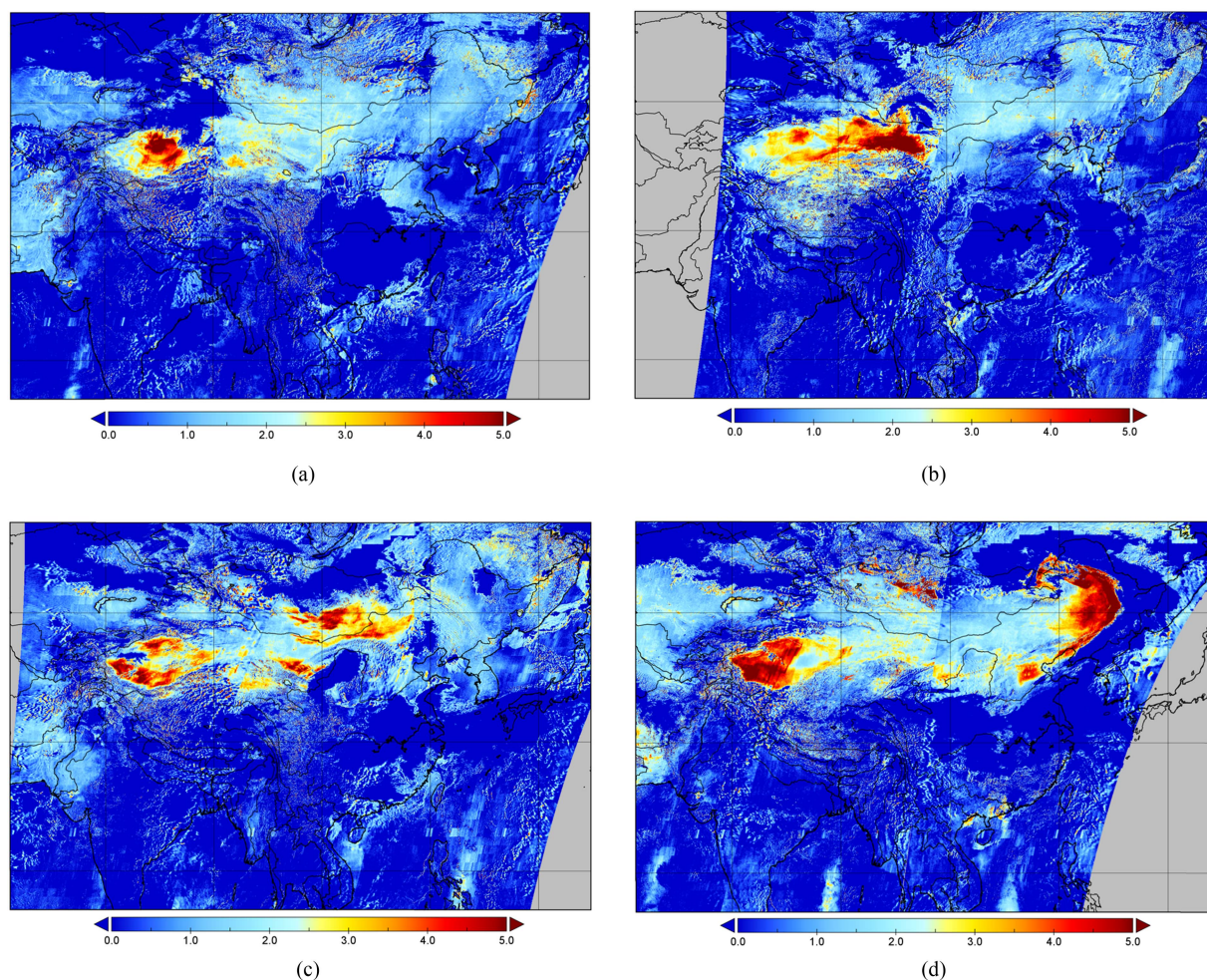
Fig. 8(a)–(d) illustrates the progression of severe dust pollution in the region.

Fig. 8(a) shows that the pollution event commenced in the desert region of Xinjiang on March 19, and a significant portion of the area had high or extremely high values (above 5). As evident in the distribution of pollutants on March 20, depicted in Fig. 8(b), the pollution event originated in the desert region of Xinjiang. By the time the satellite passed over the area on March 20, dust pollutants had already been transported to the east for a long distance and reached the vicinity of Gansu, where the AAI index registered an exceptionally high value, and a substantial area attained a relatively uncommon level above 5.

As depicted in Fig. 8(c), the transport of pollutants persisted in an easterly direction on March 21, exhibiting a somewhat dispersed distribution of dust. Notably, a substantial quantity of dust has been observed in Mongolia. A significant amount of dust remained in Ningxia and Gansu, whereas a portion of the dust was situated in the northern region of Inner Mongolia. The AAI values in the region where dust was prevalent were elevated, with a vast area encompassing to 4–5 or higher values. Dust pollution in Mongolia has reached a critical level in recent years, extending its impact to border regions and northern China [37], [38].

As depicted in Fig. 8(d), a sandstorm event occurred at multiple locations across North China and Northeast China on March 22. Although certain regions in Northeast China have experienced severe sandstorm conditions, the topographic and meteorological conditions in Beijing and its surrounding areas have also resulted in significant pollution [39], [40]. Furthermore, the majority of northern China is subjected to varying levels of pollution.

C. Dust Pollution Across China in April 2023

Fig. 9(a)–(f) depicts the national distribution of AAI observed by AAS for several successive days during the occurrence of sustained pollution events throughout the country in April. After April 10, severe sandstorms occurred in the northern region of China, particularly around Beijing, and in the following days, extreme dust or floating dust weather also occurred, which significantly affected people's daily lives and posed a threat to their health [41], [42].

On April 7, as depicted in Fig. 9(a), the primary source of dust was Xinjiang, and the AAI values indicated that a substantial portion of the region exceeded the highest threshold of the general standard 5, exhibiting an eastward trend. Fig. 9(b) from April 8 illustrates that the dust spread eastward from Xinjiang
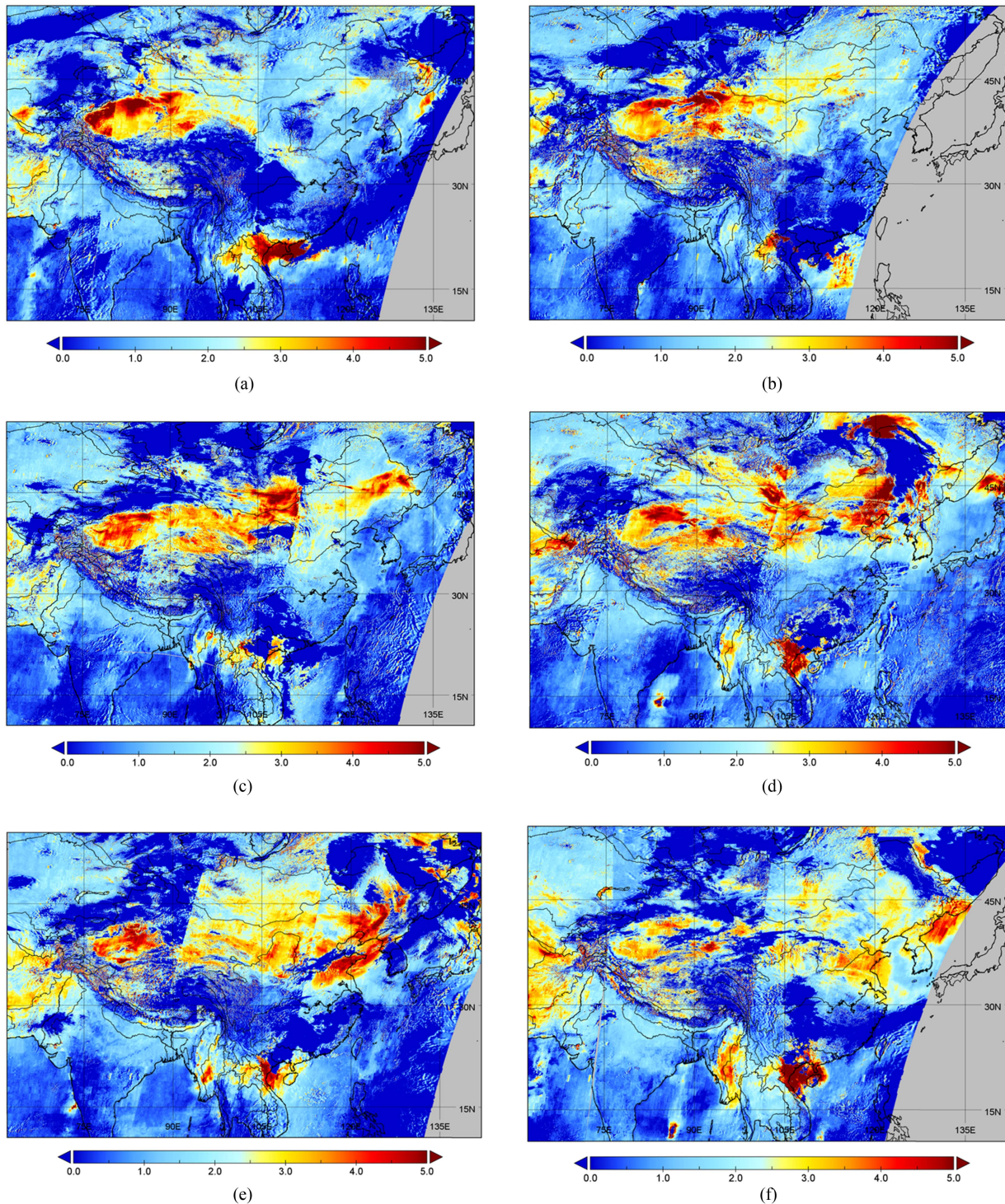
Fig. 9.   AAS observed the nationwide pollution process in China from April 7 to April 12, 2023. (a)–(f) Are for April 7–12, respectively.

over a certain distance, with the highest value area shifting to the border region of Gansu and Inner Mongolia. Additionally, a steady stream of dust continued to be transported into the atmosphere within the Taklimakan Desert. Furthermore, a noteworthy dust distribution was observed in the Mongolian Plateau, with numerous areas displaying AAI values of approximately 3.

As shown in Fig. 9(c), the expansion of the dust area on April 9 proceeded eastward, with the highest concentration of

dust evident in Mongolia and Inner Mongolia. According to previous studies, Mongolia accounts for more than 42% of the dust concentrations in Northern China during March and April [43], [44]. Moreover, severe pollution was observed in parts of Northeast China, with the AAI value of 5 in a significant area. Some dust was also present in North China, where the value ranged from 2 to 3, and a substantial amount of dust approached this region.
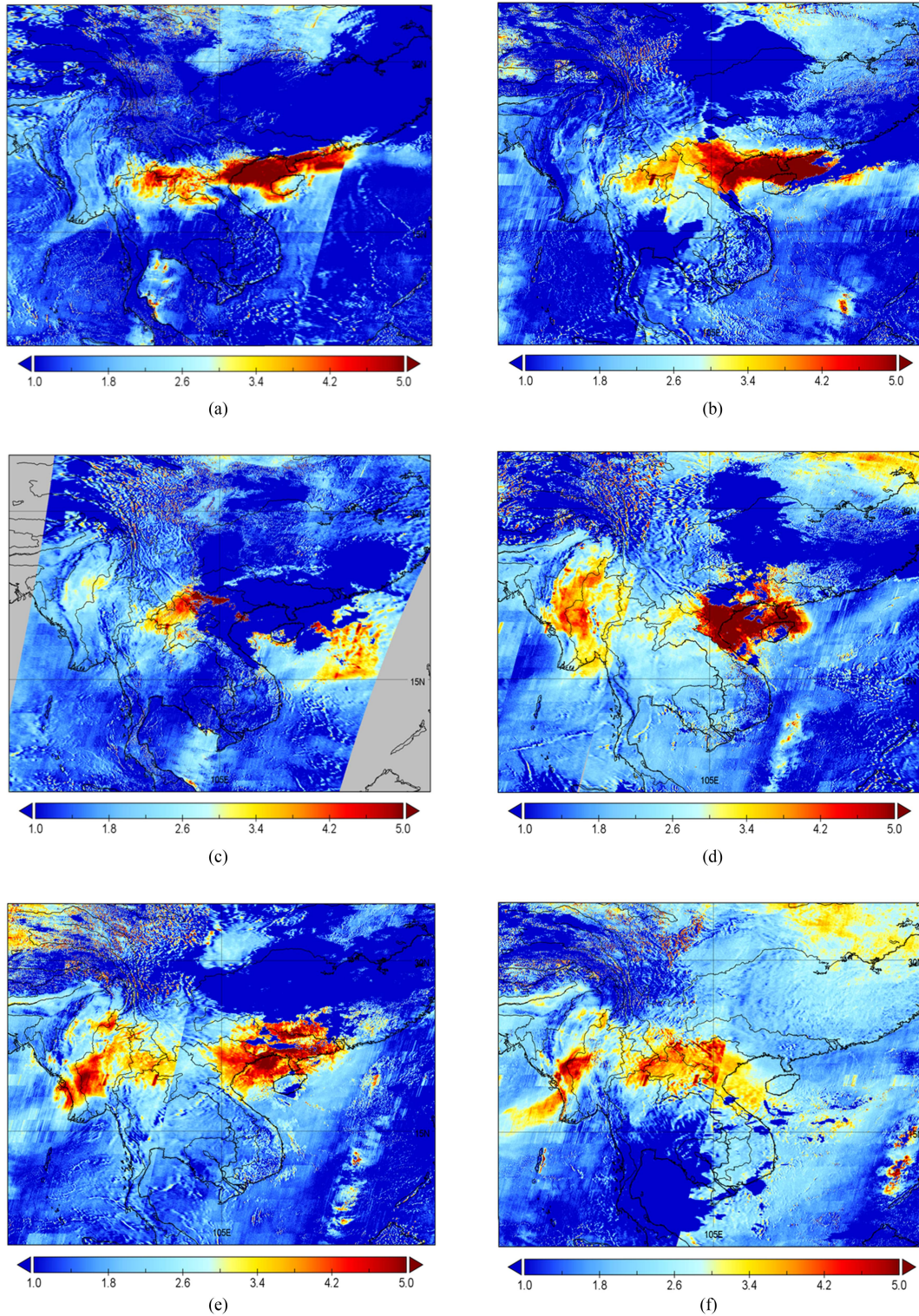
Fig. 10. AAI distribution from AAS in the Indochina Peninsula on April 6, 7, 8, 12, 14, and 16, 2023. (a)–(f) Are for April 6, 7, 8, 12, 14, and 16, respectively.

Fig. 9(d) depicts the extensive arrival of a severe sandstorm that encompassed northern China on April 10. The values recorded were primarily between 4 and 5, with some areas exceeding 5. Additionally, the northeastern region experienced significant pollution, despite the majority of areas being shrouded by thick clouds. Notably, some areas with minimal cloud coverage or only a few clouds also registered high values of approximately 5.

Fig. 9(e) demonstrates that a substantial quantity of dust pollution traversed Shandong on April 11 and progressed to Anhui and Jiangsu, and the high AAI region from 4 to 5 moved southward significantly. Similarly, Fig. 9(f) illustrates that the

Fig. 11.   AAI for Canada wildfire on June 22, 2023, from AAS.

dust event on the 12th intensified further to the southeast, and the Yangtze River Delta region endured severe air pollution, which has not been commonly observed in the area.
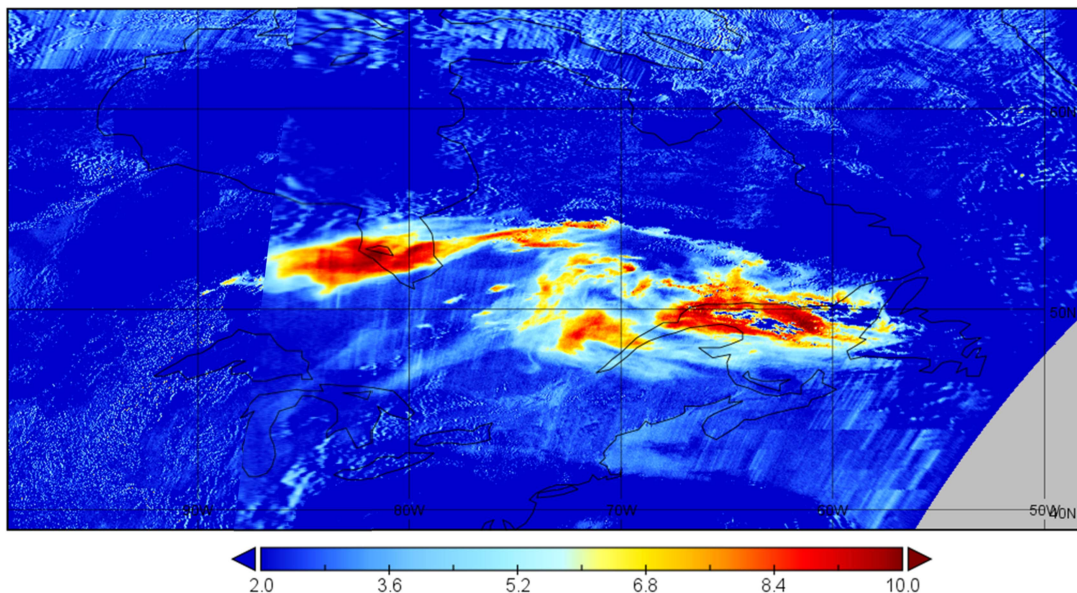
D. April 2023 Pollution in Indochina Peninsula

The Indochina Peninsula is characterized by a tropical monsoon climate. During the dry spring season, the region is susceptible to large-scale wildfires, which are often caused by a combination of natural and anthropogenic factors. Some of these fires are sparked by natural phenomena, such as lightning strikes or droughts, while others are the result of human activities, such as land burning or garbage burning. These cases produce large quantities of smoke and ash, which are then carried by low-altitude southwest winds and spread to the northeast, eventually reaching numerous locations throughout southern China.

In April 2023, the pollution generated in the Indochina Peninsula had a severe effect on the air quality of the surrounding areas, and the pollutants were transported eastward, causing significant consequences in Yunnan, Hainan, Guangxi, Guangdong, and the South China Sea.

On April 6 [Fig. 10(a)], pollutants were produced in numerous locations across the Indochina Peninsula and subsequently transported eastward toward China. The following day, on April 7 [Fig. 10(b)], the pollutants continued to be transported in an easterly direction, covering the entire Qiongzhou Strait and most areas of Hainan Island.

On April 8 [Fig. 10(c)], the pollutants persisted in their migration toward the South China Sea. Despite the absence of any visible reduction in the sources of pollution, the affected region in southern China continued to expand and endure for several consecutive days.

On April 12 [Fig. 10(d)], the Beibu Gulf region experienced a significant accumulation of extremely high levels of pollutants, simultaneously observing extensive zones of high-value pollution throughout Myanmar.

On April 14 [Fig. 10(e)], pollutants in the Beibu Gulf and southern China exhibited a propensity for dispersion. Two days later, on April 16 [Fig. 10(f)], a noticeable inclination toward spreading westward toward the Indian Ocean was observed.

Based on these findings, the pollution event lasted over 10 days. Compared with the dust pollution experienced in northern China during the same period, pollution in Southeast Asia displayed distinct traits of multipoint dispersion and persistence. However, the pollution did not travel great distances, and there was no clearly defined transmission path.

We chose four AERONET sites from four different countries which are shown in Fig. 1. The four sites are the Luang Namtha site in Laos, the Dhaka University site in Bangladesh, the Silpakom University site in Thailand, and the Bac Lieu site in Vietnam.

Fig. 12(a) in the Appendix depicts the daily averaged SDA 500 nm AOD observed at the Luang Namtha site in Laos, indicating several days of relatively high pollution in April. The figure also shows the SDA 500 nm Fine Mode Fraction of the site, demonstrating that most particles were in the Fine mode, with some coarse mode particles still present, likely introduced by natural factors.

Fig. 12(b) in the Appendix depicts the daily averaged SDA 500 nm AOD observed at the Dhaka University site in Bangladesh, which indicated that the air pollution levels in this region were high during April 6–15. The figure also shows the SDA 500 nm Fine Mode Fraction of the site, demonstrating that the majority of air pollution particles were in the Fine mode, suggesting that they were primarily produced by combustion processes. Fig. 12(c) in the Appendix depicts the daily averaged SDA 500 nm AOD observed at the Silpakom University site in Thailand, and it also displays the SDA 500 nm Fine Mode Fraction of the site. In contrast, Fig. 12(d) in the Appendix shows the daily averaged SDA 500 nm AOD observed at the Bac Lieu site in Vietnam, and illustrates the SDA 500 nm

Fine Mode Fraction at that site. Despite differing occurrence times of high AOD values compared with the Laos station, the main pollution components at these sites were Fine mode particles. This confirms that the primary pollutants in this area are anthropogenic or natural biomass combustion rather than dust. This demonstrates that the AAS can observe various types of absorbing aerosols beyond dust.

E. Canadian Wildfires on June 22, 2023

During the late May and early June periods of 2023, numerous wildfires across the central and eastern regions of the United States resulted in significant air pollution. In late June, the prevailing atmospheric circulation facilitated the movement of soot in an easterly direction. Fig. 11, sourced from the AAS, depicts the AAI for Canadian wildfires on June 22, 2023. It demonstrated a clear correlation between the distribution of pollution particles and the distribution of pollutants, as illustrated by the MODIS true color-corrected reflectance from that same day (Fig. 13 in Appendix). The MODIS true color-corrected reflectance is captured from https://worldview.earthdata.nasa.gov/?v=12.942206399289148,31.537983391586906204.7774665148961,68.7089278624063&t=2023-06-22-T06%3A21%3A47Z.

V. CONCLUSION

This study served as a pioneering effort in employing AAI products derived from the AAS to trace multiple aerosol pollution incidents after AAS in orbit. We used data from March 29 and 31 and April 3, 4, 5, and 7, 2024 of merged data from MetOp-B/GOME-2 and MetOp-C/GOME-2 in 23W–60E and 10S–51N, which is around the Sahara Desert to evaluate the accuracy of AAS observation results. The AAS data were projected onto a $1° \times 1°$ grid of GOME-2 and then averaged. The correlation coefficients between GOME-2 and AAS results in the 6 days were all about 0.8, and the mean value was 0.8127, indicating that the results of AAS are reliable.

The investigation conducted on March 4, 2022, by comparing the AAI data from AAS with TROPOMI observations of local pollution in the Bohai Sea, revealed consistent results and comparable spatial resolution. Data from AAS were used to analyze the pollution distribution of large-area dust pollution in China during March and April 2023. The application of AOD data from AERONET to authenticate the AAS observations of pollution events over the Central Asian Peninsula in April 2023 demonstrated the utility of AAS in tracking aerosol pollution. The correlation analysis between global AAI distribution data and GOME-2 on April 11, 2023 verified the accuracy of the AAS observations for multiple types of pollution. Finally, we employed the AAI derived from the AAS to investigate the distribution of burning particles during the Canadian wildfires on June 22, 2023. Illustrative cases have demonstrated the capacity of AAI from the AAS to effectively observe and track absorbing air pollution particles.
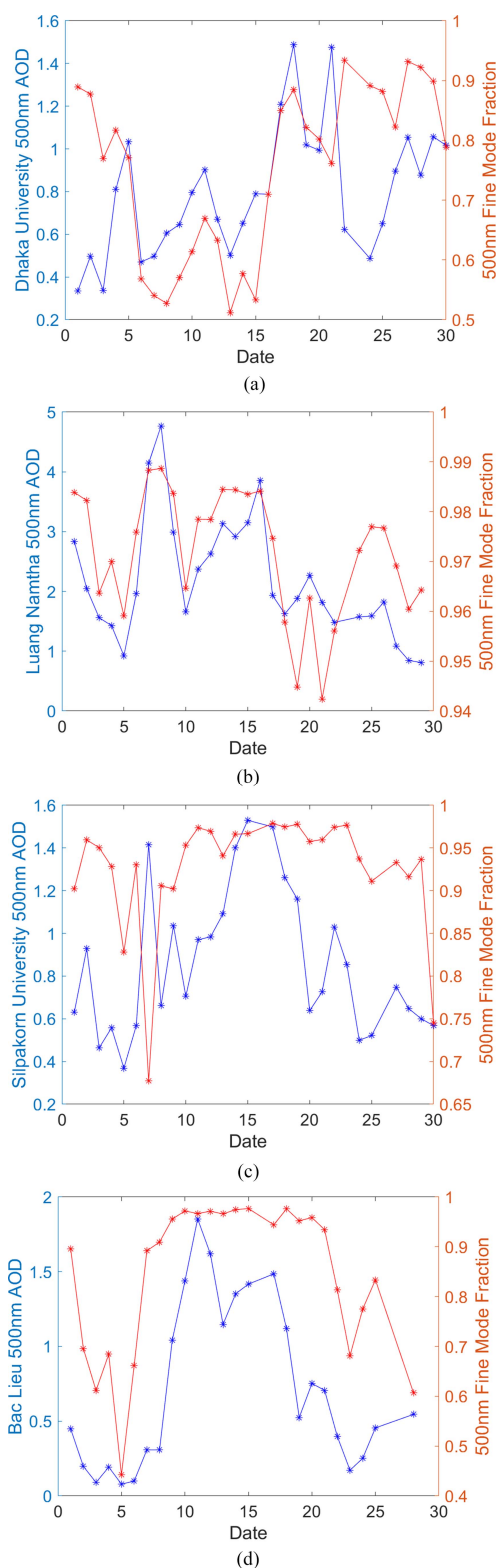
Fig. 12. (a) AERONET level 1.5 daily averaged SDA 500 nm AOD and 500 nm Fine Mode Fraction of Luang Namtha site in Laos in April, 2023. (b) AERONET level 1.5 daily averaged SDA 500 nm AOD and 500 nm Fine Mode Fraction of Dhaka University site in Bangladesh in April, 2023. (c) AERONET level 1.5 daily averaged SDA 500 nm AOD and 500 nm Fine Mode Fraction of Silpakom University site in Thailand in April, 2023. (d) AERONET level 1.5 daily averaged SDA 500 nm AOD and 500 nm Fine Mode Fraction of Bac Lieu site in Vietnam in April, 2023.

Fig. 13.   MODIS true color-corrected reflectance map for Canada wildfire on June 22, 2023.

VI. DISCUSSION

There are aspects of the AAI inversion for the AAS that require improvement. For example, the cloud parameters used for deduction were not sufficiently precise, which led to the appearance of slight, colored, discrete spots in the AAI images over complex terrains. Additionally, stripes often appeared on the product images that were 1° in length along the track direction. This was because the background used for deduction had a 1° resolution along the longitudinal direction, which was too coarse for a nadir spatial resolution of 4 km. More accurate backgrounds will be updated in the future.

AAI is a parameter sensitive to the instrument degradation and in-orbit calibration. Therefore, it can be used to monitor the in-orbit running condition of the instrument and evaluate the effect of onboard calibration work. Because years of long-term AAI record could provide a method to evaluate changes in atmospheric environment condition and radiation budget, it can be used in the analysis of environmental and radiation variations. Also, AAI is an important indicator and auxiliary in the retrieval of AOD and other trace gases. In this aspect, AAI from AAS also could be used to improve the retrieval of other instruments on the same satellite. Meanwhile, data from other payloads onboard the GaoFen-5B could also be used to improve the retrieval accuracy of AAS by imported into the retrieval model. The method and results can also be used in the atmospheric composition retrieval of subsequent payloads.

Declaration of Competing Interest: The authors declare that they have no known competing financial interests or personal relationships that could have influenced the work reported in this study.

APPENDIX

See Figs. 12 and 13.

REFERENCES

[1] E. W. Butt et al., "The impact of residential combustion emissions on atmospheric aerosol, human health, and climate," *Atmospheric Chem. Phys.*, vol. 16, no. 2, pp. 873–905, 2016.

[2] J. Cheng et al., "Pathways of China's PM2.5 air quality 2015–2060 in the context of carbon neutrality," *Nat. Sci. Rev.*, vol. 8, no. 12, 2021, Art. no. nwab078.

[3] H. Che et al., "Aerosol optical and radiative properties and their environmental effects in China: A review," *Earth-Sci. Rev.*, vol. 248, 2023, Art. no. 104634.

[4] M. O. Andreae, C. D. Jones, and P. M. Cox, "Strong present-day aerosol cooling implies a hot future," *Nature*, vol. 435, no. 7046, pp. 1187–1190, Jun. 2005.

[5] C. Hong et al., "Weakening aerosol direct radiative effects mitigate climate penalty on Chinese air quality," *Nature Climate Change*, vol. 10, no. 9, pp. 845–850, 2020.

[6] Y. J. Kaufman, D. Tanré, and O. Boucher, "A satellite view of aerosols in the climate system," *Nature*, vol. 419, no. 6903, pp. 215–223, 2002.

[7] M. De Graaf, P. Stammes, O. Torres, and R. B. A. Koelemeijer, "Absorbing Aerosol Index: Sensitivity analysis, application to GOME and comparison with TOMS," *J. Geophys. Res.: Atmos.*, vol. 110, no. D1, pp. 372–384, 2005.

[8] J. V. Dave, "Effect of aerosols on the estimation of total ozone in an atmospheric column from the measurements of its ultraviolet radiance," *J. Atmos. Sci.*, vol. 35, no. 5, pp. 899–911, 1978.

[9] I. Chiapello, J. M. Prospero, J. R. Herman, and N. C. Hsu, "Detection of mineral dust over the North Atlantic Ocean and Africa with the Nimbus 7 TOMS," *J. Geophys. Res.: Atmos.*, vol. 104, no. D8, pp. 9277–9291, 1999.

[10] F. Bednarz, *GOME Global Ozone Monitoring Experiment Users Manual.* Paris: European Space Agency, 1995.

[11] S. Noel et al., "Nadir, limb, and occultation measurements with SCIAMACHY," *Adv. Space Res.*, vol. 29, no. 11, pp. 1819–1824, 2002.

[12] P. Levelt and R. Noordhoek, *OMI Algorithm Theoretical Basis Document (ATBD. OMI-01, Version, No. 1).* USA: OMI, 2002.

[13] L. E. Flynn, C. J. Seftor, J. C. Larsen, and P. Xu, "The ozone mapping and profiler suite," in *Earth Science Satellite Remote Sensing*, vol. 1, J. J. Qu, W. Gao, M. Kafatos, R. E. Murphy, and V. V. Salomonson, Eds. Heidelberg, Germany: Springer, 2006, pp. 279–296.

[14] J. P. Veefkind et al., "TROPOMI on the ESA Sentinel-5 precursor: A GMES mission for global observations of the atmospheric composition for climate, air quality and ozone layer applications," *Remote Sens. Environ.*, vol. 120, pp. 70–83, 2012.

[15] M. De Graaf and P. Stammes, "SCIAMACHY Absorbing Aerosol Index–calibration issues and global results from 2002–2004," *Atmospheric Chem. Phys.*, vol. 5, no. 9, pp. 2385–2394, 2005.

[16] L. Tilstra, M. De Graaf, I. Aben, and P. Stammes, "In-flight degradation correction of SCIAMACHY UV reflectances and Absorbing Aerosol Index," *J. Geophys. Res.: Atmos.*, vol. 117, no. D6, 2012, Art. no. D06209.

[17] Q. L. Kleipool, M. R. Dobber, J. de Haan, and P. F. Levelt, "Earth surface reflectance climatology from 3 years of OMI data," *J. Geophys. Res.: Atmos.*, vol. 113, no. D18, 2008, Art. no. D18308.

[18] M. De Graaf, O. Tuinder, and L. G. Tilstra, "O3MSAF algorithm theoretical basis document for ARS," in *O3MSAF/KNMI/ATBD/002.* De Bilt, The Netherlands: Koninklijk Nederlands Meteorologisch Instituut, 2010, pp. 1–26.

[19] W. Wang et al., "Cross-calibration of the total ozone unit (TOU) with the ozone monitoring instrument (OMI) and SBUV/2 for environmental applications," *IEEE Trans. Geosci. Remote Sens.*, vol. 50, no. 12, pp. 4943–4955, Dec. 2012.

[20] W. Wang et al., "Introduction to the FY-3A total ozone unit: Instrument, performance and results," *Int. J. Remote Sens.*, vol. 32, no. 17, pp. 4749–4758, 2011.

[21] W. H. Wang et al., "Analysis for retrieval and validation results of FY-3 total ozone unit (TOU)," *Chin. Sci. Bull.*, vol. 55, pp. 3037–3043, 2010.

[22] Y. M. Wang et al., "FY-3 satellite ultraviolet total ozone unit," *Chin. Sci. Bull.*, vol. 55, pp. 84–89, 2010.

[23] X. Zhang, L. Wang, W. Wang, D. Cao, X. Wang, and D. Ye, "Long-term trend and spatiotemporal variations of haze over China by satellite observations from 1979 to 2013," *Atmos. Environ.*, vol. 119, pp. 362–373, 2015.

[24] Z. Zhang, Y. Wang, W. Wang, and H. Wang, "Sensitivity study of viewing path and spectral resolution on Absorbing Aerosol Index," *Chin. J. Space Sci.*, vol. 39, no. 1, pp. 93–99, 2019.

[25] F. Tang, W. Wang, F. Si, H. Zhou, Y. Luo, and Y. Qian, "Successful derivation of Absorbing Aerosol Index from the environmental trace gases monitoring instrument (EMI)," *Remote Sens*, vol. 14, no. 16, 2022, Art. no. 4105.

[26] J. Mao, Y. Wang, E. Shi, X. Hu, Q. Wang, and J. Wang, "Pre-launch multi-energy radiance calibration of the OMS-N," *Remote Sens*, vol. 16, no. 1, 2023, Art. no. 119.

[27] J. Mao, Y. Wang, E. Shi, and J. Wang, "Pre-launch spectral calibration of the absorbed aerosol sensor," *Sensors*, vol. 23, no. 20, 2023, Art. no. 8590.

[28] G. Meister et al., "The ocean color instrument (OCI) on the plankton, Aerosol, cloud, ocean ecosystem (PACE) mission: System design and prelaunch radiometric performance," *IEEE Trans. Geosci. Remote Sens.*, vol. 62, Apr. 2024, Art. no. 5517418, doi: 10.1109/TGRS.2024.3383812.

[29] Y. Wang et al., "In-flight preliminary performance of GF-5B/Absorbing Aerosol Sensor," *Remote Sens*, vol. 15, no. 17, 2023, Art. no. 4343.

[30] J. R. Herman, P. K. Bhartia, O. Torres, C. Hsu, C. Seftor, and E. Celarier, "Global distribution of UV-absorbing aerosols from Nimbus 7/TOMS data," *J. Geophys. Res.: Atmos.*, vol. 102, no. D14, pp. 16911–16922, 1997.

[31] V. Rozanov, A. Rozanov, A. A. Kokhanovsky, and J. Burrows, "Radiative transfer through terrestrial atmosphere and ocean: Software package SCIATRAN," *J. Quantitative Spectrosc. Radiative Transfer*, vol. 133, pp. 13–71, 2014.

[32] L. G. Tilstra, O. N. E. Tuinder, and P. Stammes, "GOME-2 Absorbing Aerosol Index: Statistical analysis, comparison to GOME-1 and impact of instrument degradation," in *Proc. EUMETSAT Meteorological Satell. Conf.*, Cordoba, Spain, 2010.

[33] O. Torres, H. Jethva, C. Ahn, G. Jaross, and D. G. Loyola, "TROPOMI aerosol products: Evaluation and observations of synoptic scale carbonaceous aerosol plumes during 2018–2020," *Atmospheric Meas. Techn. Discuss.*, vol. 13, pp. 6789–6806, 2020.

[34] M. L. Kooreman et al., "Effects of clouds on the UV Absorbing Aerosol Index from TROPOMI," *Atmospheric Meas. Tech.*, vol. 13, pp. 6407–6426, 2020.

[35] V. V. Salomonson, W. L. Barnes, P. W. Maymon, H. E. Montgomery, and H. Ostrow, "MODIS: Advanced facility instrument for studies of the Earth as a system," *IEEE Trans. Geosci. Remote Sens.*, vol. 27, no. 2, pp. 145–153, Mar. 1989.

[36] X. Xiong, B. N. Wenny, and W. D. Barnes, "Overview of NASA Earth observing systems terra and aqua moderate resolution imaging spectroradiometer instrument calibration algorithms and on-orbit performance," *J. Appl. Remote Sens.*, vol. 3, no. 1, 2009, Art. no. 032501.

[37] T. Bao, T. Gao, B. Nandintsetseg, M. Yong, and E. Jin, "Variations in frequency and intensity of dust events crossing the Mongolia–China border," *Sola*, vol. 17, pp. 145–150, 2021.

[38] O. Vova, M. Kappas, T. Renchin, J. Degener, and N. Action, "Land degradation assessment in Gobi-Altai province," in *Proc. Building Resilience Mongolian Rangelands: Trans-Disciplinary Res. Conf.*, 2015, pp. 54–59.

[39] J. Liu, L. Xue, X. Huang, Z. Wang, S. Lou, and A. Ding, "Intensified haze formation and meteorological feedback by complex terrain in the North China Plain region," *Atmospheric Ocean. Sci. Lett.*, vol. 16, no. 2, 2023, Art. no. 100273.

[40] X. Zhang, J. Zhong, J. Wang, Y. Wang, and Y. Liu, "The interdecadal worsening of weather conditions affecting aerosol pollution in the Beijing area in relation to climate warming," *Atmospheric Chem. Phys.*, vol. 18, no. 8, pp. 5991–5999, 2018.

[41] S. E. Bauer, U. Im, K. Mezuman, and C. Y. Gao, "Desert dust, industrialization, and agricultural fires: Health impacts of outdoor air pollution in Africa," *J. Geophys. Res.: Atmos.*, vol. 124, no. 9, pp. 4104–4120, 2019.

[42] W. J. Requia, H. Amini, R. Mukherjee, D. R. Gold, and J. D. Schwartz, "Health impacts of wildfire-related air pollution in Brazil: A nationwide study of more than 2 million hospital admissions between 2008 and 2018," *Nature Commun.*, vol. 12, no. 1, 2021, Art. no. 6555.

[43] S. Chen et al., "Mongolia contributed more than 42% of the dust concentrations in Northern China in March and April 2023," *Adv. Atmospheric Sci.*, vol. 40, no. 12, pp. 1549–1557, 2023.

[44] Z. Yin, Y. Wan, Y. Zhang, and H. Wang, "Why super sandstorm 2021 in North China?," *Nat. Sci. Rev.*, vol. 9, no. 3, 2022, Art. no. nwab165.

Jian Xu (Senior Member, IEEE) received the B.E. degree in geographic information systems from Hohai University, Nanjing, China, in 2004, and the M.S. degree in Earth-oriented space science and technology and the Ph.D. degree in atmospheric remote sensing from Technische Universita¨t Mu¨nchen, Munich, Germany, in 2009 and 2015, respectively.

From 2010 to 2021, he was with the Remote Sensing Technology Institute, German Aerospace Center, Oberpfaffenhofen, Germany. He was involved in the development/refinement of atmospheric retrieval algorithms for ESA's Sentinel-5P and Sentinel-4 satellite missions. He is currently a Professor with the National Space Science Center, Chinese Academy of Sciences, Beijing, China. His research interests include remote sensing of planetary atmosphere, radiative transfer modeling, and ill-posed inverse problems.

Yongmei Wang received the Ph.D. degree in space physics from the Center for Space Science and Applied Research, Chinese Academy of Sciences, Beijing, China, in 2003.

She is a doctoral supervisor with the National Space Science Center, Laboratory of Space Environment Exploration. She is interested in optical remote sensing for atmosphere and space weather. Since 2001, she has worked in the field of development of optical instruments for atmospheric trace gas and aerosol measurement. She has been responsible for the Total Ozone Unit (TOU) onboard the FengYun-3B/C, the Absorbing Aerosol Sensor (AAS) on Gao-Fen 5B, and Hyperspectral Ozone Map Sensor-Nadir (OMS-N) on the FenYun-3F meteorological satellite. She is also the Project Manager of the Ultraviolet Imager (UVI) on SMILE satellite.

Entao Shi received the B.S. degree in applied physics from Harbin University of Science and Technology, Harbin, China, in 2005, the M.S. degree in optical engineering from Beijing Institute of Technology, Beijing, China, in 2010, and the Ph.D. degree in optical remote sensing from the Chinese Academy of Science, Beijing, in 2018.

Since 2010, he has been an Associate Researcher with the National Space Science Center, Chinese Academy of Science. Since then, he has been engaged in meteorological satellite payload instrument development including optical system design, mechanical design, alignment, etc. He is currently working on the AAS project on Gao-Fen 5B and Ozone Monitoring Suite-nadir (OMS-N) on the FenYun-3F meteorological satellite.

Zhuo Zhang received the B.S. degree in applied physics from Jilin University, Changchun, China, in 2013, and the Ph.D. degree in space environment exploration from the Chinese Academy of Sciences, Beijing, China, in 2018.

She is currently an Assistant Research Fellow with the National Space Science Center, Chinese Academy of Sciences. She works in optical remote sensing instrument on-board calibration and aerosol retrieval.

Pengfei Zhang received the master's degree in microelectronics and solid-state electronics from the South China University of Technology, Guangzhou, China, in 2013.

He is currently an Engineer with Shanghai Institute of Satellite Engineering, and is mainly engaged in remote sensing work. His research focuses mainly on microwave remote sensing technology and optical remote sensing technology.

Shun Yao received the M.S. degree in photogrammetry and remote sensing from Wuhan University, Wuhan, China, in 2018.

He is currently an Engineer with DFH Satellite Company, Ltd., Beijing, China. He has authored or coauthored more than five refereed articles published in journals and conferences proceedings. His research interests include satellites' optical payload design and remote sensing image processing.

Jun Zhu received the M.S. degree in physical electronics from Tianjin University, Tianjin, China, in 2003.

He has more than 20 years of experience in system design of optical remote sensing satellite. He is currently a Research Professor with DFH Satellite Company, Ltd., Beijing, China, and serves as the Director of the General Research Laboratory of Optical Remote Sensing Satellite System Design Department. He has authored or coauthored more than 15 refereed articles published in journals and conferences proceedings. His research interests include optical remote sensing and satellite design.

Mr. Zhu was the recipient of the Second-Class Prizes of the State Scientific and Technological Progress Award.

Lanlan Rao received the master's degree in cartography and geographic information engineering from the China University of Mining and Technology (CUMT), Xuzhou, China, in 2017, and the Ph.D. degree in atmospheric remote sensing from the Technical University of Munich (TUM), Munich, Germany, in 2022.

From 2017 to 2022, she was with the Remote Sensing Technology Institute (IMF), the German Aerospace Center (DLR), Weßling, Germany. Since 2023, she has been with the National Space Science Center (NSSC), the Chinese Academy of Sciences (CAS), Beijing, China. Her research focuses on the remote sensing of aerosol properties using satellite data.

Houmao Wang received the master's degree in environmental science from the Yantai Institute of Coastal Zone Research, Chinese Academy of Sciences (CAS), Yantai, China, in 2011, and the Ph.D. degree in detection of earth and space from the National Space Science Center, CAS, Beijing, China, in 2017.

He is currently an Associate Professor of optical remote sensing with the National Space Science Center, CAS. He has authored or coauthored more than 40 refereed articles published in journals. His research interests include remote sensing of the wind field and temperature of the middle and upper atmosphere, intercalibration of the radiance of spectrometer (e.g., TROPOMI, GOME2, OMPS, OMS, and AAS), data processing of L0\L1 satellite instrument, etc.

Dr. Wang has undertaken many research or engineering projects, including the 863 Program, National Natural Science Foundation of China, Key Research and Development Program of the Ministry of Science and Technology, National Engineering Models. He is the Deputy Chief Designer of GF5 (2) Satellite UV Absorption Aerosol Detector and FY-3 (6) Satellite Hyperspectral Detector for National Engineering Model Tasks.

Jinghua Mao received the Ph.D. degree in space environment exploration from the Chinese Academy of Sciences, Beijing, China, in 2017.

She is currently an Associate Researcher with the National Space Science Center, Chinese Academy of Sciences. She is working on the alignment and calibration of satellite instruments. She is currently working as an Instrument Scientist of the Ozone Monitoring Suite-nadir (OMS-N) onboard the Chinese FengYun-3F meteorological satellite and in charge of the alignment and calibration. She has been also working on the AAS project on Gao-Fen 5B.